Molecular mechanism of RUVBL1/2-TTT complex assembly by GNB1L

Authors: Junfei Guo[1†], Guangxian Wang[1†], Weiwang Tang[1], Zexuan Zheng[1], Zihan Zhang[1], Junxiang Cui[1], Gang Cai[1,2*], Xuejuan Wang[1*]

Affiliations:

[1] Department of Radiation Oncology, the First Affiliated Hospital of USTC, MOE Key Laboratory for Cellular Dynamics, Center for Advanced Interdisciplinary Science and Biomedicine of IHM, Division of Life Sciences and Medicine, University of Science and Technology of China, Hefei, Anhui, China 230027.

[2] Key Laboratory of Anhui Province for Emerging and Reemerging Infectious Diseases, Hefei, Anhui, China.

[†] These authors contributed equally to this work.

* Correspondence: Xuejuan Wang (xuejuan@ustc.edu.cn) and Gang Cai (gcai@ustc.edu.cn)

Abstract

Acting as dedicated co-chaperones, the AAA+ ATPases RUVBL1/2 and the TTT (TTI1-TTI2-TELO2) complex facilitate the maturation and assembly of phosphatidylinositol 3-kinase-related kinases (PIKKs), 270-470 kDa kinases critical for cellular homeostasis. However, the mechanisms governing RUVBL1/2-TTT assembly, the role of ATP hydrolysis, and the function of regulators like GNB1L remain unclear. Here we determined the cryo-EM structures of the full-length human TTT-RUVBL1/2-GNB1L complex in multiple functional states. The architecture reveals a 16-subunit assembly with three head-to-tail-linked TTT copies and a RUVBL1/2 hexamer in an asymmetric, mixed-nucleotide state. Unexpectedly, GNB1L adopts a tilted orientation to directly engage three Switch Loops of RUVBL1, tethering it to two ordered TELO2 protomers. We demonstrate that GNB1L, together with TTT, acts as a conformational hub that remodels the RUVBL1/2 ring to stimulate activity. Our findings establish that GNB1L physically integrates co-chaperone assembly while allosterically regulating its ATPase-driven chaperone function.

Introduction

Phosphatidylinositol 3-kinase (PI3K)-related kinases (PIKKs) are unconventional large (270-470 kDa) proteins and constitute an atypical family of serine/threonine kinases[1,2]. There are six members and each plays a pivotal role in controlling cellular homeostasis, including the DNA damage response (ATM, ATR, DNA-PKcs), cell growth (mTOR), mRNA decay (SMG1) and transcriptional regulation (TRRAP) [1,3]. PIKK folding and maturation critically depends on alternative or parallel pathways mediated by either the R2TP complex (RUVBL1-RUVBL2-RPAP3-PIH1D1) or the GNB1L/TTT/RUVBL1/2 machinery, which act alongside HSP90 to support the assembly of several essential multiprotein complexes[4,5], including but not limited to PIKKs, RNA polymerase II, and small nucleolar ribonucleoproteins[6-12].

RUVBL1 and RUVBL2 form a heterohexameric AAA+ ATPase complex[13,14] featuring a unique DII domain insertion; this protruding domain defines two distinct faces (the ATPase-face and DII-face) and mediates protein-protein interactions[14-16]. Up to three RPAP3 molecules can bind to the two distinct faces of RUVBL1/2 hexamer, however, only one PIH1D1 is engaged by a DII domain[17]. The RUVBL1/2 hexamer not only constitutes the core of R2-TP but also provides a structural framework for the INO80 family of chromatin remodelers[18-20]. While ATP hydrolysis plays a crucial role in the assembly and dynamic maturation of various R2TP/TTT-dependent multiprotein complexes[21], inhibition of this activity does not measurably compromise the assembly or stability of INO80-family complexes[14].

The TTT (TTI1-TTI2-TELO2) complex functions as a dedicated Hsp90 co-chaperone that is strictly required for the folding and stabilization of de novo synthesized PIKKs, and is thus essential for maintaining their kinase activity

and overall cellular function[11,22,23]. All three proteins adopt extended helical-repeat architectures: TTI1 furnishes a platform that anchors TELO2 and TTI2, while only the TELO2 C-terminal domain (CTD) remains disordered in the structure[24,25]. Functionally, the TELO2 CTD as well as N- and C-terminal segments of TTI1 directly engage distinct domains of PIKK clients[22,25]. TTT binds two consecutive DII domains within the RUVBL1/2 ring, and—unexpectedly—this interaction diminishes RUVBL1/2 ATPase activity[24], raising the question of how an ATP-dependent co-chaperone cycle can proceed when a core co-chaperone dampens enzymatic activity.

GNB1L, a recently identified component associated with TTT, promotes PIKK biogenesis, yet its molecular function has remained unclear[26,27]. *In vivo*, GNB1L interacts robustly with TELO2 and HSP90, yet no detectable contacts are formed with either the R2 (RUVBL1/2) or TP (RPAP3-PIH1D1)[26]. Asa1 is the budding-yeast ortholog of GNB1L[28]; notably, the Asa1/GNB1L-TTT axis stabilises newly synthesised PIKKs, whereas R2TP-TTT is implicated in refolding heat-denatured PIKKs, suggesting two distinct pathways that together maintain PIKK proteostasis: an R2-GNB1L route and an R2TP route[29]. Consistent with this view, emerging evidence suggests that certain functions attributed to R2TP may not strictly require RPAP3 and PIH1D1[14]. GNB1L and Asa1 are WD40 repeat proteins whose structural integrity is essential, as deletion of any single WD repeat phenocopies complete loss of GNB1L, resulting in reduced PIKK abundance and impaired proliferation[26].

Assembly of a functional RUVBL1/2-TTT complex represents a pivotal regulatory step in PIKK biogenesis[14,21].However, in the absence of structural information placing GNB1L within the R2-TTT framework, it is therefore not clear whether and how GNB1L promotes RUVBL1/2-TTT assembly, and how

the ATPase cycle is harnessed in this context. Here, we determined the dynamic architectures of the full-length human TTT-RUVBL1/2-GNB1L co-chaperone complex purified and imaged in the absence of exogenous nucleotides. Unlike previous cryo-EM structures of RUVBL1/2-TTT, where TTT bound peripherally to the RUVBL1/2 hexamer with high flexibility and limited resolution[24], our TTT-RUVBL1/2-GNB1L structure shows that GNB1L stabilizes three head-to-tail TTT protomers on the RUVBL1/2 hexamer, promoting assembly and significantly enhancing ATPase activity. This stabilization enabled improved resolution, revealing the TELO2 CTD and its interactions with TTI1, GNB1L, and RUVBL2 for the first time, and allowed correction of the TTI2 N- and C-terminal orientations proposed in earlier low-resolution models. Moreover, asymmetric transitions in nucleotide occupancy-ATP/ADP binding in RUVBL1 coupled to ADP exchange in RUVBL2-drive a conserved hinge-like rotation of the DII domain, extensively reshaping TTT conformations and likely tuning its engagement with PIKK clients. Together, these findings illuminate how co-chaperone assembly and ATPase-driven allostery are integrated within the HSP90-PIKK maturation cycle.

Results

Overall architecture of the TTT-RUVBL1/2-GNB1L complex

To elucidate how GNB1L regulates assembly of the RUVBL1/2-TTT complex and to establish a rapid and robust pipeline for large-scale preparation, we reconstituted the human TTT-RUVBL1/2-GNB1L complex using the MultiBac baculovirus expression system [30]. Following anti-FLAG affinity purification and size-exclusion chromatography (SEC), we obtained a highly homogeneous sample (Extended Data Fig. 1). Using single-particle cryo-electron microscopy (cryo-EM), we determined an overall reconstruction at 3.36 Å resolution, revealing a characteristic “three-leaf clover” architecture. Two-dimensional classification showed well-defined features in the core, whereas peripheral densities were comparatively diffuse, indicating substantial conformational flexibility of the peripheral TTT modules (Extended Data Fig. 2). To mitigate this heterogeneity, we applied a local refinement strategy, improving the resolution of the central RUVBL1/2 heterohexameric ring and the peripheral GNB1L-TTT module to 3.17 Å and 3.9 Å, respectively (Extended Data Fig. 3). These maps enabled construction of a complete atomic model comprising the RUVBL1/2 hexamer, three TTT subcomplexes, and a single GNB1L molecule.

The assembled TTT-RUVBL1/2-GNB1L measures ~230 Å × 230 Å × 140 Å and exhibits pronounced pseudo-C3 symmetry. The RUVBL1/2 heterohexamer forms the central basal platform, whereas GNB1L stabilises three head-to-tail TTT protomers on the RUVBL1/2 ring (Fig. 1a). The outward-projecting DII domains of RUVBL1 and RUVBL2 constitute the principal scaffolding elements that capture and position the three peripheral TTT subcomplexes. Notably, the complex displays a modular assembly logic: each TTT subcomplex engages tightly with one RUVBL1/2 heterodimer to form a basic structural unit; three such units are arranged with ~120° rotational

symmetry and are linked in a head-to-tail manner to generate the stable holoenzyme (Fig. 1a).

GNB1L is located at the centre of the bottom face of the complex and adopts a "bearing"-like configuration, being tightly encased by the C-terminal regions of two TELO2 subunits (Fig. 1a, bottom view). This distinctive positioning suggests that GNB1L serves as a central hub that connects and coordinates subunit assembly. Guided by the atomic model, we further mapped key structural motifs and interface residues onto linear sequence schematics, providing a domain-level functional framework for each subunit and for their interaction surfaces (Fig. 1b).

Nucleotide-binding states and conformational plasticity of the RUVBL1/2 hexameric ring

Previous biochemical preparations of the human RUVBL1/2 complex included defined exogenous nucleotides, and the reported ring structures are almost invariably nucleotide-bound, with the three RUVBL1 and three RUVBL2 subunits typically displaying identical nucleotide occupancy[14]. Whether ATP hydrolysis by RUVBL1/2 plays a specific role in complex assembly has remained unclear. In contrast, no exogenous nucleotides were added during our preparation of the TTT-RUVBL1/2-GNB1L complex; Nonetheless, the 3.36 Å consensus cryo-EM map revealed a predominant binding pattern characterized by ATP in the three RUVBL1 subunits and ADP in the three RUVBL2 subunits. To strictly validate this assignment and eliminate potential model bias, we performed map refinement/reconstruction after removing all nucleotides from the reference map. The clear density signals corresponding to ATP and ADP were faithfully recovered, confirming the reliability and

objectivity of our map (Extended Data Fig. 5d). Specifically, local resolution estimation of the R2 hexamer (~3.2 Å overall) showed that the stable ATP-binding sites reached 2.5-3.0 Å, where ATP molecules fit remarkably well into the density (Extended Data Fig. 5a-c). In contrast, the ADP-binding sites exhibited higher flexibility with local resolutions of 3.0-3.5 Å, yet still accommodated ADP comfortably. All subsequent assignments of ATP and ADP followed these exact criteria. (Extended Data Fig. 5e-f).

To resolve nucleotide-occupancy heterogeneity in the RUVBL1/2 complex, we employed a two-pronged classification strategy. First, we performed iterative rounds of focused 3D classification in cryoSPARC using a mask encompassing the hexameric ring (Extended Data Figs. 3, 4,6). In parallel, we carried out continuous heterogeneity analysis with the deep learning-based algorithm cryoDRGN (Extended Data Figs. 3,7,8). Together, these complementary approaches effectively resolved the nucleotide-occupancy heterogeneity, enabling us to define four distinct nucleotide-occupancy states.: an all-ADP state (all six subunits bound to ADP); a 1ATP-4ADP-1apo state (the second RUVBL1 copy ATP-bound, and the second RUVBL2 copy apo); a 1ATP-3ADP-2apo state (the first RUVBL1 copy ATP-bound, with the second and third RUVBL2 copies apo); and a 2ATP-4ADP state (the second and third RUVBL1 copies ATP-bound) (Fig. 2a; Extended Data Fig. 9). Across these states, the gross geometry of the RUVBL1/2 ring remained essentially constant (outer diameter ~122 Å; pore diameter ~27 Å). Strikingly, conformational transitions in the N-terminal region of RUVBL2 (ordered versus disordered) correlated strictly with nucleotide state: in the apo state, the RUVBL2 N-terminus became invisible in the map, consistent with disorder (Fig. 2a; Extended Data Fig. 10c). A similar pattern of order-disorder transition at the RUVBL2 N-terminus has also been reported for the RUVBL1/2-DHX34 complex[15].

Structural comparison of AAA+ active site in RUVBL1 and RUVBL2 subunits indicated that the canonical catalytic motifs (Walker A/B and Sensor I) exhibit no major rearrangements during the ATP-to-ADP transition, with only a minor ~2 Å or ~3.5 Å displacement of the DII domain in RUVBL1 and RUVBL2 (Fig. 2b, c; Extended Data Fig. 9a,b). Two RUVBL1 N-terminal histidines, H18 and H20 appeared central to this regulation: in the ATP-bound state, H18 interacts with T77 (Extended Data Fig. 10a), while H20 stabilises the adenine moiety of the nucleotide. This dual-anchoring mechanism secures the N-terminus over the nucleotide-binding pocket, creating steric hindrance that prevents release. In the ADP-bound state, the H18-T77 interaction is lost and the ADP base is no longer stabilised by H20 (Extended Data Fig. 10b). Upon ADP binding, the N-terminus maintains only weak interactions with ADP and exhibits partial disorder, with a degree of flexibility intermediate between the ATP-bound and ADP-released states (Extended Data Fig. 9c). H18 and H20 in RUVBL1 structurally and functionally correspond to H25 and H27 in RUVBL2 (Fig. 2c). The H25 and H27 residues, along with the region encompasing N-terminal residues 1-44 are disordered, which is probably due to its ADP binding or realase state. The RUVBL2 N-terminal disordering and opening a channel for ADP release are tightly coupled (Extended Data Fig. 10c).

To functionally assess the contribution of these four histidines to RUVBL1/2 ATPase activity, we generated a combined mutant of RUVBL1(H18A/H20A) and RUVBL2(H25A/H27A). Compared with wild-type RUVBL1/2, the ATPase activity of this quadruple histidine mutant is reduced by more than 70% (Figure 2d). These findings functionally demonstrate that RUVBL1(H18/H20) and RUVBL2(H25/H27) play a critical role in regulating the ATPase activity of the RUVBL1/2 complex.

Conformational dynamics of the RUVBL1/2 DII domains and the interaction network

The unique insertional DII domains of RUVBL1/2 are well established as primary mediators of protein-protein interactions[14,31]. Typically, DII adopts nucleotide-dependent conformations: an “outward” state in ADP-bound or Apo conditions, and an “inward” state in the ATP-bound state [31]. Unexpectedly, despite mixed nucleotide occupancy in our reconstructions, all DII domains in the TTT-RUVBL1/2-GNB1L complex adopt the outward conformation. Moreover, the axial heights of the RUVBL1 versus RUVBL2 DII domains differ substantially (relative height difference ~13 Å; Fig. 3a). Superposition of the AAA+ core domains revealed an ~25 Å relative displacement between the DII domains of RUVBL1 and RUVBL2 (Fig. 3b), a divergence that enables specific engagement of TTI1 by RUVBL1 and of TTI2 by RUVBL2 (Fig. 3c).

In contrast to the previously described R2-TTT binding mode, in which one TTT protomer is anchored by two consecutive DII domains (Extended Data Fig. 11), we observed a distinct configuration in the TTT-RUVBL1/2-GNB1L complex: three consecutive DII domains-derived from one RUVBL1/2 heterodimer plus a neighbouring RUVBL2-jointly tether a single TTT copy (Fig. 3c; Extended Data Fig. 11). Accordingly, the DII domains provide the principal anchoring platform for R2-TTT assembly through three key interfaces: (i) the RUVBL2 DII ring (residues 209-226) inserts into the helical solenoid surface of TTI2 (HEAT 4R, 202-214; HEAT 5R, 240-257; HEAT 6R, 288-301) (Fig. 3c-i); (ii) two regions of RUVBL1 DII (residues 168-173 and 194-199) recognise and bind an extended peptide segment of TTI1 (residues 442-456) (Fig. 3c-ii); (iii) the apex region of RUVBL2 DII (residues 148-158 and 169-174) interacts with the C-terminal HEAT 16R of TELO2 (residues 791-831) (Fig. 3c-iii). These

extensive and specific interfaces collectively ensure precise assembly and stable positioning of the TTT subcomplex on the RUVBL1/2 scaffold.

To probe the structural remodelling mechanism, we compared RUVBL1/2 in the TTT-RUVBL1/2-GNB1L complex with RUVBL1/2-containing chromatin remodellers, including TIP60, INO80, and SRCAP (PDB: 9C57, 7ZI4, 8X15) (Fig. 3d; Extended Data Fig. 12). I In these remodellers, the RUVBL1/2 ring adopts a closed state with an outer diameter of ~114 Å, wherein the RUVBL1 Switch Loop (residues 250–270; located within the DII core) occludes the central pore—a structural feature consistent with the inhibitor-bound state of the RUVBL1/2 ring (Fig. 3e, upper panel; Extended Data Fig. 13). By contrast, the TTT-RUVBL1/2-GNB1L complex exhibits an open ring with an outer diameter of ~122 Å (Fig. 3e, lower panel).

This difference is primarily driven by a marked rearrangement of the RUVBL1 Switch Loop. In the previously solved R2-TTT complex[24], the Switch Loop is disordered due to high dynamics (PDB: 7OLE; EMD-12979). In our structure, the Switch Loop and DII undergo concerted movements: Switch Loop repositioning relieves pore occlusion (Fig. 3e, lower panel), while DII transitions from the inward conformation characteristic of chromatin remodellers to the outward conformation. This coordinated motion both opens the pore and creates the steric space required to accommodate GNB1L binding (Fig. 3f).

To elucidate the mechanisms of structural remodeling, we compared the RUVBL1/2 ring within the TTT–RUVBL1/2–GNB1L complex to those in other RUVBL1/2-containing chromatin remodeling complexes, including TIP60, INO80, and SRCAP. Notably, compared to isolated RUVBL1/2, the structural features of RUVBL1/2 within these assemblies likely reflect distinct conformational changes induced by their respective complex-specific subunits.

Nevertheless, these comparisons reveal an important allosteric principle: in chromatin remodellers, the RUVBL1/2 ring can be ADP-bound while adopting a DII conformation typically associated with the ATP state (Extended Data Fig. 12); conversely, in the TTT-RUVBL1/2-GNB1L complex, DII remains outward despite mixed nucleotide states. Thus, within assembled complexes, DII conformation is not dictated solely by nucleotide occupancy but is strongly shaped by interacting co-chaperones and adaptors such as GNB1L (Fig. 3f). Through high conformational plasticity of the DII domain and Switch Loop, the RUVBL1/2 scaffold can specifically recognize and engage diverse adaptor proteins[4].

Structural basis of TTT assembly and its conformational regulation

Our cryo-EM structure of the TTT-RUVBL1/2-GNB1L complex clearly reveals three TTT units assembled in a head-to-tail manner on a single RUVBL1/2 ring, with the TTT region resolved to 3.9 Å. In the R2–TTT reconstruction previously reported by Pal et al., three bound TTT complexes were observed per hexameric R2 ring. To achieve higher local resolution, symmetry expansion was applied to focus on a single RUVBL1/2 pair, yielding a structural model with density for TTT at approximately 9 Å resolution. However, the structural details provided by this model were limited. .

At this 3.9 Å resolution, we resolved intra- and inter-TTT interface in detail. TTI1 and TELO2 form a tight intra-TTT interface mediated by hydrophobic packing and an extensive hydrogen-bonding network (Fig. 4a, inset i; Extended Data Fig. 14). The C-terminus of TTI1 interacts primarily via electrostatics with the C-terminus of TTI2, thereby stabilizing each individual TTT copy (Fig. 4a, inset ii). At the inter-TTT interface between adjacent TTT

copies, the N-terminus of TTI1 extends outward to contact the N-terminus of the neighbouring TTI2; specifically, HEAT 2-3R of TTI1 mediates a head-to-tail linkage with HEAT 1R of the adjacent TTI2 (Fig. 4a). The interactions among the three TTT copies are mediated by the N-termini of TTI2 and TTI1, with varying interaction strengths between the copies (dashed circles in Fig. 4a), suggesting that the TTT copies exhibit structural plasticity during oligomerization.

Our structure unambiguously reveals that the spatial orientation of TTI2 within the TTT complex is completely opposite to that of the previously published TTT models[24,25]. We systematically validated the orientation of TTI2 and its interaction with TTI1 in the following three ways: Firstly, approximately 35% of the TTI2 subunit exhibits side-chain density of sufficient quality to unambiguously identify bulky residues (Figure 4b) and multiple helical pairs within residues 245-420 of TTI2 (Figure 4c), allowing us to build this region de novo. Secondly, our model reveals that the N- and C- termini of TTI2 form stable interactions with two TTI1 copies via complementary electrostatic networks (Figure 4a-ii; Extended Data Fig. 15a). The strong electrostatic complementarity, which would be disrupted by the reversed orientation seen in earlier models (Extended Data Fig. 15b), provides compelling support the correctness of our TTI2 termini assignment. Furthermore, we performed functional validation of the TTI2-TTI1 interaction interface by comparing the co-purification behavior of wild-type TTI2, an N-terminal truncation (Δ1-100), and a C-terminal truncation (Δ302-508) with TELO2 and TTI1. Both wild-type TTI2 and the N-terminal truncation formed stable complexes with TELO2 and TTI1, whereas the C-terminal truncation failed to bind them stably (Figure 4d). These results indicate that the TTI2 C-terminus is critical for stable association with TELO2 and TTI1, functionally validating the structural TTI2-TTI1 interface and corroborating the accuracy of our TTI2 termini assignment.

We further resolved the structure of the TELO2 C-terminal domain (CTD; residues 515-624 and 696-837) for the first time (Fig. 4e; Extended Data Fig.15d). The TELO2-CTD not only remains tightly associated with TTI1 (Extended Data Fig. 14e) but also extends outward to directly engage the RUVBL2 DII domain and GNB1L (Fig. 4e-i,ii). Among the three TTT copies, the TELO2-CTD of two copies (copy 1 and 2) binds GNB1L, whereas the CTD of the third copy (copy 3) is disordered and the corresponding TTT copy is highly unstable (Fig. 1b). Specifically, $TELO2_1$-CTD segments (791-807 and 811-837) directly interact with $RUVBL2_3$-DII (148-158) (Fig. 4e-i), and $TELO2_1$-CTD core region (562-572) directly contacts GNB1L (Fig. 4e-ii, Extended Data Fig.16b). Notably, the TELO2-CTD of copy 2 displays pronounced conformational dynamics, undergoing an order–disorder transition and dynamically associating with GNB1L (Fig. 4f).

To validate whether CTD fragment (562-572) plays a key role in mediating the interaction with GNB1L, we truncated the fragment of TELO2. Compared with full-length wild-type TELO2, the TELO2 CTD (Δ563-571) mutant shows a reduced interaction with GNB1L and concomitantly weakens RUVBL1 binding within the TTT-RUVBL1/2-GNB1L complex, suggest that the TELO2 CTD fragment contributes to stabilizing TELO2-GNB1L association (Fig. 4g). Although AlphaFold predictions and previous studies suggest that TELO2 residues 498–505 bind GNB1L, this region appears disordered in our cryo-EM structure. Thus, TELO2 likely engages GNB1L via two distinct interfaces: the ordered 562–572 segment provides stable binding, whereas the flexible 498–505 region may mediate transient and dynamic interactions.

Structural and functional role of GNB1L in TTT-RUVBL1/2-GNB1L complex

GNB1L is a canonical WD40 repeat protein comprising seven β-propeller repeats. Previous work showed that deletion of any single WD40 repeat substantially weakens the interaction between GNB1L and TELO2 and causes severe reductions in cellular PIKK levels [26]. To define the mechanistic basis by which GNB1L regulates the TTT-RUVBL1/2 complex, we analyzed its spatial localization and the interfaces it mediates. Unexpectedly, GNB1L inserts into a bottom groove of the RUVBL1/2 hexamer at an ~45° tilt (Fig. 5a). This specific tilt appears to arise from a mechanically balanced interplay between three RUVBL1 Switch Loops and the pulling forces exerted by two TELO2 CTDs (Fig. 5b,c).

GNB1L WD40 repeats 2, 3, and 5 directly engage the Switch Loop regions (residues 250-270) of the three RUVBL1 subunits (Fig. 5b). In chromatin remodellers, the Switch Loop typically occupies a position that blocks the central pore (Fig. 3e); in our structure, GNB1L binding forces the Switch Loops to move laterally away from the pore axis, thereby opening the central channel. Previous studies further reported that deletion of WD40 repeats 6-7 markedly reduces GNB1L association with HSP90 [26]. Consistent with this, repeats 1-5 are buried within the complex, whereas repeats 6-7 are exposed on the exterior and face the disordered CTD region (Extended Data Fig. 16a), suggesting that exposed repeats 6-7 could provide a binding platform for HSP90.

GNB1L also acts as a “molecular glue” for TTT assembly, by directly interacting with the two TELO2 CTDs, which were disordered in all previously reported complexes (Fig. 5c, d; Extended Data Fig. 17a). WD40 repeat 1 interacts with the TELO2-CTD (residues 562-572) of the second TTT copy (TTT-Copy2), whereas repeats 4, 5, and 7 bind the TELO2-CTD of the first TTT copy (TTT-Copy1) (Fig. 5c,d; Extended Data Fig. 16b). In contrast, the

third TTT copy does not engage GNB1L and its TELO2-CTD remains disordered. Through these interactions, GNB1L physically links and stabilizes the first two TTT copies, establishing itself as an indispensable adaptor for R2-TTT assembly (Fig. 1b; Fig. 5c).

Comparative analysis further showed that GNB1L binding substantially remodels the overall R2-TTT architecture. Relative to the previously reported R2-TTT structure (PDB: 7OLE; EMD-12979), incorporation of GNB1L not only stabilizes the assembly of three TTT units on the RUVBL1/2 ring but also shifts the TTT modules outward by ~8 Å relative to RUVBL1/2 (Extended Data Fig. 17b). Moreover, GNB1L alters RUVBL1/2 ring geometry: the outer diameter increases from ~115 Å to ~122 Å and the pore diameter expands from ~22 Å to ~27 Å, yielding a pronounced breathing-like expansion (Extended Data Fig. 17c).

We systematically delineated the role of GNB1L within the TTT-RUVBL1/2-GNB1L complex through a series of biochemical, structural, and functional experiments. Single-molecule mass photometry showed that, in a system containing only RUVBL1/2-TTT, the RUVBL1/2 hexamer predominantly binds a single TTT, with assembly of three TTT copies being extremely rare; upon addition of GNB1L, particles stably bearing three TTT copies increased dramatically and became the dominant assembly state (Fig. 5e), and pull-down assays likewise confirmed that GNB1L enhances the interaction between RUVBL1/2 and TTT (Fig. 5g). *In vitro* ATPase assays further demonstrated that TTT alone does not activate RUVBL1/2 ATPase activity, whereas GNB1L alone exerts only a moderate stimulatory effect; in the intact TTT-RUVBL1/2-GNB1L complex, however, GNB1L and TTT synergistically and robustly enhance RUVBL1/2 ATPase activity, and

supplementing GNB1L into the RUVBL1/2-TTT system similarly causes a strong increase in ATPase activity (Fig. 5f, left).

Structural analysis revealed that the RUVBL1 Switch Loop constitutes the key interface for GNB1L binding (Fig. 5b). This loop undergoes substantial conformational rearrangements that either impose or relieve occlusion of the central pore of the RUVBL1/2 hexamer (Fig. 3f). Notably, deletion of the Switch Loop in the RUVBL1/2-TTT system markedly increases ATPase activity (Fig. 5f, right), indicating that the Switch Loop exerts an autoinhibitory effect on the RUVBL1/2 hexamer, consistent with previous observations [32]. Moreover, in the presence of wild-type RUVBL1, GNB1L further enhances ATPase activity, whereas it has almost no effect on the Switch Loop deletion mutant (Fig. 5f, right). Together, these results indicate that the RUVBL1 Switch Loop inhibits RUVBL1/2 ATPase activity, and that GNB1L activates the ATPase primarily by alleviating this Switch Loop-mediated inhibition.

The cryoDRGN heterogeneity analysis further revealed that GNB1L binding correlates with TTT stability-particles with intact GNB1L density exhibit tighter TTT association, whereas those lacking GNB1L show looser binding-demonstrating that GNB1L promotes cooperative assembly of three TTT copies on the RUVBL1/2 ring (Extended Data Fig. 8).

Collectively, these biochemical, structural, and functional lines of evidence demonstrate that GNB1L is bifunctional: on the one hand, it acts as a critical structural “stabilizer” of the TTT-RUVBL1/2-GNB1L complex by promoting the cooperative assembly of three TTT copies on the RUVBL1/2 hexameric ring; on the other hand, it serves as an indispensable catalytic activator that stimulates RUVBL1/2 ATPase activity.

Discussion

GNB1L as a central hub for RUVBL1/2-TTT assembly and allosteric control

In contrast to prior R2-TTT structures suggesting that one TTT complex stably binds one RUVBL1/2 hexamer [24], our study identifies GNB1L as the principal structural organiser of the R2-TTT assembly. GNB1L not only mediates physical recruitment of three TTT copies onto a single RUVBL1/2 ring but also activates RUVBL1/2 ATPase activity through multivalent interactions and allosteric effects. Structurally, GNB1L inserts into the RUVBL1/2 ring at an ~45° tilt, a geometry that enables simultaneous anchoring of the DII-domain Switch Loop and two TELO2-CTDs from the stably bound TTT copies. This multivalent interaction network explains why formation of the complete 16-subunit holoenzyme is strictly dependent on GNB1L and provides a direct structural rationale for PIKK instability upon loss of GNB1L function.

Regulation of RUVBL1/2 ATPase activity: a conformational transition from autoinhibition to activation

R2TP function relies on ATP hydrolysis, yet the R2TP-TTT structure indicated that TTT itself diminishes RUVBL1/2 ATPase activity [24]. Our data explain how GNB1L resolves this apparent paradox through a precisely tuned allosteric mechanism. First, GNB1L “locks” the Switch Loop to initiate allostery. The RUVBL1 Switch Loop (residues 250-270) is deeply embedded in the DII core and appeared disordered in the prior R2-TTT structure due to high dynamics. GNB1L directly binds and stabilises this region, fixing its conformation and triggering long-range allosteric signalling. Second, GNB1L drives a

breathing-like expansion that optimizes catalysis. Whereas the RUVBL1/2 hexamer typically resides in a closed ground state (outer diameter ~114 Å), GNB1L binding forces the Switch Loop and DII to promote transition to an open conformation (outer diameter ~122 Å), improving nucleotide-pocket geometry and facilitating nucleotide exchange and turnover. Third, GNB1L enables energy coupling and mechanical work. GNB1L engages the switch loop of RUVBL1 to facilitate ATP hydrolysis-driven chemical energy release, which stabilizes TTT and drives the outward "flinging" motion of all six DII domains to create room for TTT binding, thereby promoting overall TTT assembly. Concurrently, the dynamic assembly of TTT feeds back to further reinforce the association of GNB1L with both RUVBL1/2 and TTT.. Through this reciprocal coupling mechanism, GNB1L functions not merely as an adaptor but as a critical allosteric activator that breaks TTT-mediated autoinhibition and initiates the ATPase cycle driving conformational remodelling and maturation of PIKK substrates.

Two independent pathways-R2-GNB1L and R2TP-support PIKK folding and maturation

In vivo studies indicate that GNB1L associates tightly with TELO2 and HSP90, yet no direct contacts with R2 (RUVBL1/2) or TP (RPAP3-PIH1D1) have been detected [26]. In budding yeast, the GNB1L/Asa1-TTT axis primarily stabilizes newly synthesized (de novo) PIKKs, whereas R2TP-TTT is specialized for refolding heat-denatured PIKKs [29], suggesting that PIKK stability is governed by two distinct but complementary pathways: an R2-GNB1L pathway and an R2TP pathway. Evolutionary evidence supports this model: fission yeast naturally lacks TP proteins and therefore relies exclusively on the R2-GNB1L route to maintain PIKK homeostasis [29]. Consistent with this, accumulated literature indicates that certain functions originally attributed to R2TP do not

strictly require TP proteins [14]. Our structures provide a molecular basis for the independence of these pathways in mammals: structural superposition shows that PIH1D1 and GNB1L competitively occupy the same binding site on the RUVBL1 Switch Loop (Extended Data Fig. 18)[4,24]. The extensive overlap of these interfaces imposes strict mutual exclusion, ensuring that cells can selectively recruit distinct adaptor proteins to discriminate between—and activate—two independent chaperone pathways.

Acknowledgements

This work was supported by the National Natural Science Foundation of China (32030057, 32271255, and 31922035), Research Funds of Center for Advanced Interdisciplinary Science and Biomedicine of IHM (QYZD20220001), the Strategic Priority Research Program of the Chinese Academy of Sciences (XDB37010000), and the Fundamental Research Funds for the Central Universities (WK9100000032). Cryo-EM data were collected at the First Affiliated Hospital of Anhui Medical University. We thank Dr. Yiyang Jiang (The First Affiliated Hospital of Anhui Medical University) for technical assistance and Dr. Yue Qin (National Institute of Biological Sciences, Beijing) for kindly providing the plasmids.

Author Contributions

X.W. conceptualized and supervised the project with input from G.C. J.G. expressed and purified protein samples and designed and performed supplementary functional assays. J.G. and W.T. jointly carried out ATPase

activity measurements and single-molecule mass photometry. Z.Z. and J.C. contributed to protein purification for ATPase assays, with assistance from W.T.Z.Z prepared the cryo-EM grids. J.G. collected the cryo-EM data. G.W. performed 3D reconstruction and atomic model building. J.G. and G.W. prepared the figures. X.W. and G.C. analyzed the data and wrote the manuscript. All authors reviewed and approved the final manuscript.

Author information

These authors contributed equally: Junfei Guo, Guangxian Wang.

Data availability

The density maps and structural coordinates of the global R2-GNB1L-TTT complex (EMDB EMD-68074; PDB 21XP) and the composite map (EMDB EMD-68073) are deposited in the EMDB and PDB. The accession codes for the distinct conformational states are as follows: state D4T2 (EMDB EMD-68126; PDB 21ZU); state A1D4T1 (EMDB EMD-68154; PDB 22BL); state D6 (EMDB EMD-68136; PDB 22AN); and state A2D3T1 (EMDB EMD-68080; PDB 21XV). All data are available in the main text or Extended Data.

Conflict of interest

The authors declare no competing interests.

References

1. Abraham, R.T. PI 3-kinase related kinases: 'big' players in stress-induced signaling pathways. *DNA Repair (Amst)* **3**, 883-7 (2004).
2. Perry, J. & Kleckner, N. The ATRs, ATMs, and TORs are giant HEAT repeat proteins. *Cell* **112**, 151-5 (2003).
3. Bakkenist, C.J. & Kastan, M.B. Initiating cellular stress responses. *Cell* **118**, 9-17 (2004).
4. Martino, F. et al. RPAP3 provides a flexible scaffold for coupling HSP90 to the human R2TP co-chaperone complex. *Nat Commun* **9**, 1501 (2018).
5. Zhao, Y. et al. Genome-scale mapping of DNA damage suppressors through phenotypic CRISPR-Cas9 screens. *Mol Cell* **83**, 2792-2809 e9 (2023).
6. Boulon, S. et al. The Hsp90 chaperone controls the biogenesis of L7Ae RNPs through conserved machinery. *J Cell Biol* **180**, 579-95 (2008).
7. Cloutier, P. et al. R2TP/Prefoldin-like component RUVBL1/RUVBL2 directly interacts with ZNHIT2 to regulate assembly of U5 small nuclear ribonucleoprotein. *Nat Commun* **8**, 15615 (2017).
8. Horejsi, Z. et al. CK2 phospho-dependent binding of R2TP complex to TEL2 is essential for mTOR and SMG1 stability. *Mol Cell* **39**, 839-50 (2010).
9. Kim, S.G. et al. Metabolic stress controls mTORC1 lysosomal localization and dimerization by regulating the TTT-RUVBL1/2 complex. *Mol Cell* **49**, 172-85 (2013).
10. Machado-Pinilla, R., Liger, D., Leulliot, N. & Meier, U.T. Mechanism of the AAA+ ATPases pontin and reptin in the biogenesis of H/ACA RNPs. *RNA* **18**, 1833-45 (2012).
11. Takai, H., Xie, Y., de Lange, T. & Pavletich, N.P. Tel2 structure and function in the Hsp90-dependent maturation of mTOR and ATR complexes. *Genes Dev* **24**, 2019-30 (2010).
12. Zhao, R. et al. Molecular chaperone Hsp90 stabilizes Pih1/Nop17 to maintain R2TP complex activity that regulates snoRNA accumulation. *J Cell Biol* **180**, 563-78 (2008).
13. Mao, Y.Q. & Houry, W.A. The Role of Pontin and Reptin in Cellular Physiology and Cancer Etiology. *Front Mol Biosci* **4**, 58 (2017).
14. Dauden, M.I., López-Perrote, A. & Llorca, O. RUVBL1-RUVBL2 AAA-ATPase: a versatile scaffold for multiple complexes and functions. *Curr Opin Struct Biol* **67**, 78-85 (2021).
15. López-Perrote, A. et al. Regulation of RUVBL1-RUVBL2 AAA-ATPases by the nonsense-mediated mRNA decay factor DHX34, as evidenced by Cryo-EM. *Elife* **9**(2020).
16. Serna, M. et al. CryoEM of RUVBL1-RUVBL2-ZNHIT2, a complex that interacts with pre-mRNA-processing-splicing factor 8. *Nucleic Acids Res* **50**, 1128-1146 (2022).
17. Munoz-Hernandez, H. et al. Structural mechanism for regulation of the

AAA-ATPases RUVBL1-RUVBL2 in the R2TP co-chaperone revealed by cryo-EM. *Sci Adv* **5**, eaaw1616 (2019).

18. Yang, Z. et al. Structural insights into the human NuA4/TIP60 acetyltransferase and chromatin remodeling complex. *Science* **385**, eadl5816 (2024).
19. Yu, J. et al. Structural insights into histone exchange by human SRCAP complex. *Cell Discovery* **10**, 15 (2024).
20. Zhang, M. et al. Hexasome-INO80 complex reveals structural basis of noncanonical nucleosome remodeling. *Science* **381**, 313-319 (2023).
21. Yenerall, P. et al. RUVBL1/RUVBL2 ATPase Activity Drives PAQosome Maturation, DNA Replication and Radioresistance in Lung Cancer. *Cell Chem Biol* **27**, 105-121.e14 (2020).
22. Takai, H., Wang, R.C., Takai, K.K., Yang, H. & de Lange, T. Tel2 regulates the stability of PI3K-related protein kinases. *Cell* **131**, 1248-59 (2007).
23. Toullec, D. et al. The Hsp90 cochaperone TTT promotes cotranslational maturation of PIKKs prior to complex assembly. *Cell Rep* **37**, 109867 (2021).
24. Pal, M. et al. Structure of the TELO2-TTI1-TTI2 complex and its function in TOR recruitment to the R2TP chaperone. *Cell Reports* **36**, 109317 (2021).
25. Kim, Y. et al. Structure of the Human TELO2-TTI1-TTI2 Complex. *J Mol Biol* **434**, 167370 (2022).
26. Huang, M. et al. FACS-based genome-wide CRISPR screens define key regulators of DNA damage signaling pathways. *Mol Cell* **83**, 2810-2828.e6 (2023).
27. Zhao, Y. et al. Genome-scale mapping of DNA damage suppressors through phenotypic CRISPR-Cas9 screens. *Mol Cell* **83**, 2792-2809.e9 (2023).
28. Shevchenko, A. et al. Chromatin Central: towards the comparative proteome by accurate mapping of the yeast proteomic environment. *Genome Biol* **9**, R167 (2008).
29. Goto, G.H. et al. Two separate pathways regulate protein stability of ATM/ATR-related protein kinases Mec1 and Tel1 in budding yeast. *PLoS Genet* **13**, e1006873 (2017).
30. Gupta, K. et al. MultiBac: Baculovirus-Mediated Multigene DNA Cargo Delivery in Insect and Mammalian Cells. *Viruses* **11**(2019).
31. García-Martín, C., López-Perrote, A., Boskovic, J. & Llorca, O. Mechanism of allosteric inhibition of RUVBL1-RUVBL2 ATPase by the small molecule CB-6644. *Cell Reports Physical Science* **5**(2024).
32. Gorynia, S. et al. Structural and functional insights into a dodecameric molecular machine – The RuvBL1/RuvBL2 complex. *Journal of Structural Biology* **176**, 279-291 (2011).

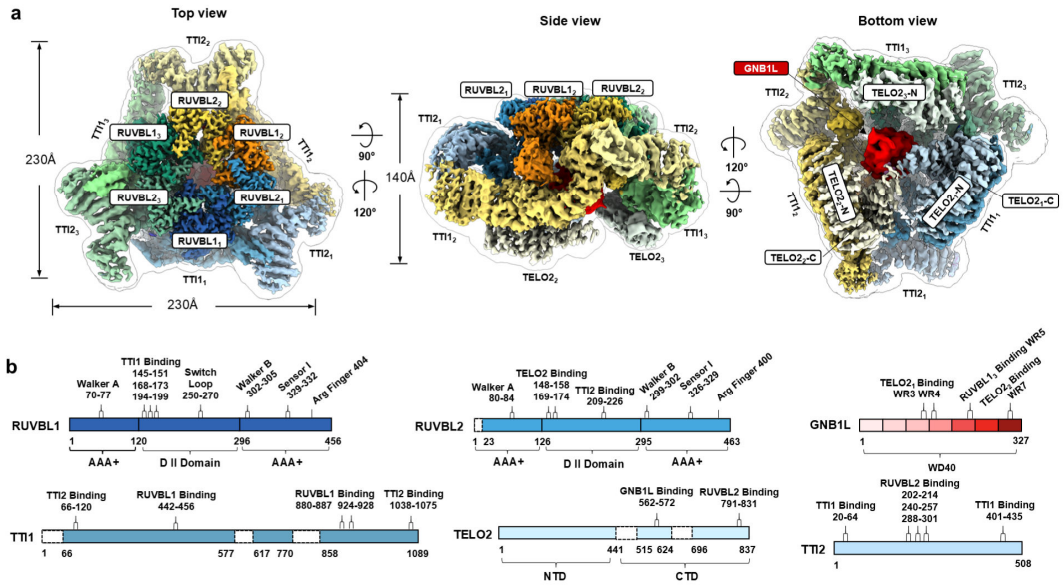

Fig.1| Overall structure of the human TTT-RUVBL1/2-GNB1L complex. a, Domain organization of individual subunits. RUVBL1, RUVBL2, TELO2, TTI1, and TTI2 are colored in blue shades and GNB1L in red. Key functional domains (AAA+ domain, DII domain, WD40 repeats) and conserved motifs (Walker A/B, arginine finger) are highlighted, with inter-subunit interaction residues annotated. **b,** Cryo-EM density map of the complex shown in three orthogonal views (top, side, and bottom), with a transparent surface envelope delineating the overall architecture. The complex exhibits pseudo-C3 symmetry, with three TELO2-TTI1-TTI2 (TTT) modules tethered to the peripheral DII domains of the heterohexameric RUVBL1/2 ring. The three symmetry-related TTT-RUVBL protomers (copies 1-3) are colored distinctly in blue, yellow, and green, respectively. Within each protomer, a color gradient distinguishes TELO2, TTI1, and TTI2, along with the associated ATPase core of the RUVBL1/2 hexamer.

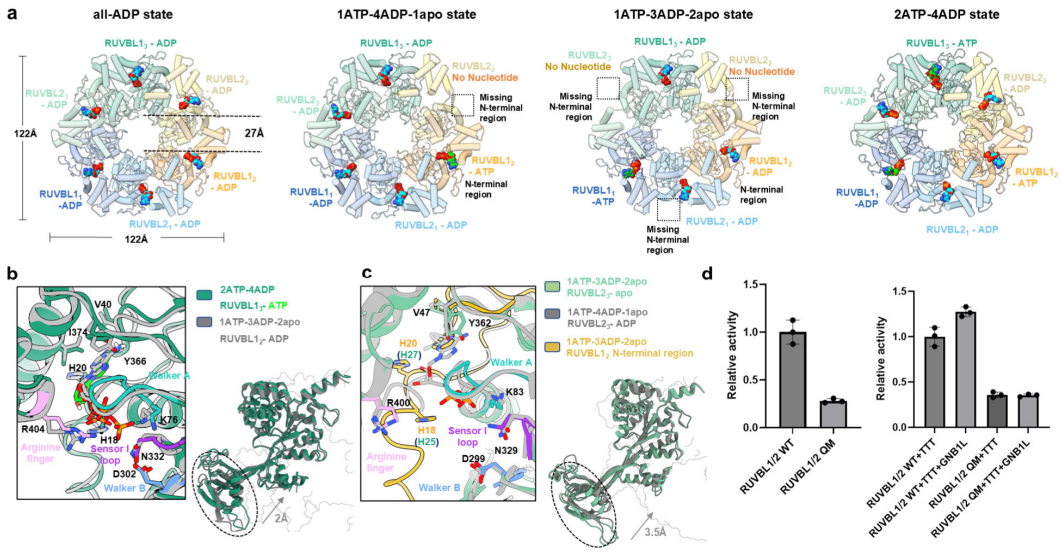

Fig.2| Nucleotide binding states of the RUVBL1/2 hexameric ring. a, Top views of four models illustrating distinct nucleotide-occupancy states of the three RUVBL1 and three RUVBL2 subunits: all-ADP, 1ATP-4ADP-1apo, 1ATP-3ADP-2apo, and 2ATP-4ADP. Bound nucleotides are shown as spheres and labeled for each subunit. The overall ring diameter and central pore aperture are indicated. Regions of missing density corresponding to the RUVBL2 N terminus are marked. **b,** Close-up view of the AAA+ active site in a representative RUVBL1 subunit, comparing the ATP-bound state (2ATP-4ADP, green) with the ADP-bound state (1ATP-3ADP2-2apo, gray). Key catalytic elements (Walker A, Walker B, sensor I loop, and the arginine finger) are highlighted in distinct colors, and representative residues (e.g., K76 and D302) are shown as side chains. The right panel depicts the relative displacement of the DII domain between these two nucleotide states. **c**, Close-up views of the AAA+ ATPase pocket in a representative RUVBL2 subunit, comparing the nucleotide-free (apo) state (1ATP-3ADP-2apo, green) with the ADP-bound state (1ATP-4ADP-1apo, grey). To facilitate visualization of N-terminal conformational changes, the N-terminal segment of the RUVBL1 subunit from the 1ATP-3ADP-2apo state is overlaid as a reference (yellow, outlined in black). Key catalytic elements (Walker A, Walker B, the sensor I loop, and the arginine finger) are highlighted in distinct colors, and representative residues

(e.g., K83 and D299) are shown as side chains. The right panel depicts the relative displacement of the DII domain between the two states. **d**, *In vitro* ATPase assays demonstrate that RUVBL1 (H18/H20) and RUVBL2 (H25/H27) residues play a critical role in regulating the ATPase activity of the RUVBL1/2 complex. Left, comparison of ATPase activity between wild-type RUVBL1/2 and the quadruple histidine mutant. Right, comparison of wild-type and quadruple histidine mutant RUVBL1/2 in the presence of the RUVBL1/2-TTT incubation mixture with or without GNB1L. Data are shown as mean values with individual data points from three technical replicates, and error bars indicate s.d.

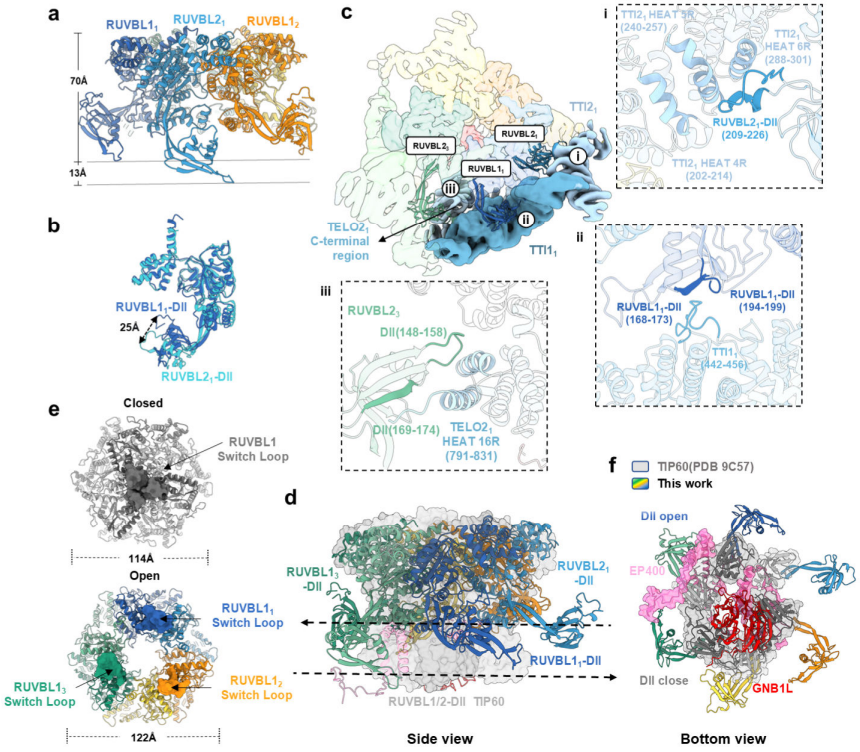

Fig.3| Conformational dynamics of the DII domains in the RUVBL1/2 hexamer. a, Side view of the RUVBL1/2 heterohexamer highlighting the DII insertion domains of RUVBL1 and RUVBL2. The relative vertical positions of the DII domains are indicated. **b,** Superposition of the AAA+ core domains of RUVBL1 and RUVBL2 showing the relative displacement of their DII domains. **c,** Interface between a single TTT subcomplex and the RUVBL1/2 DII domain. Insets i-iii show close-up views of key contacts. **d,** Comparison of the RUVBL1/2-GNB1L module in the TTT-RUVBL1/2-GNB1L complex (this study; coloured model) with the homologous RUVBL1/2-EP400 module in the TIP60 complex (PDB 9C57; grey surface at 80% transparency), after alignment of the AAA+ rings. Dashed lines indicate the cross-sections shown in panel e and f. **e,** Bottom views of the Switch Loop region within the RUVBL1/2 DII domain in the TTT-RUVBL1/2-GNB1L (bottom) and the RUVBL1/2-EP400 module in the TIP60 complex (top), highlighting conformational differences associated with

binding to distinct adaptor proteins. **f,** Bottom view of the RUVBL1/2 DII domain in the TTT-RUVBL1/2-GNB1L complex (coloured model) and the RUVBL1/2-EP400 module in the TIP60 complex (semi-transparent grey surface with fitted model). EP400 is shown in hot pink and GNB1L in red.

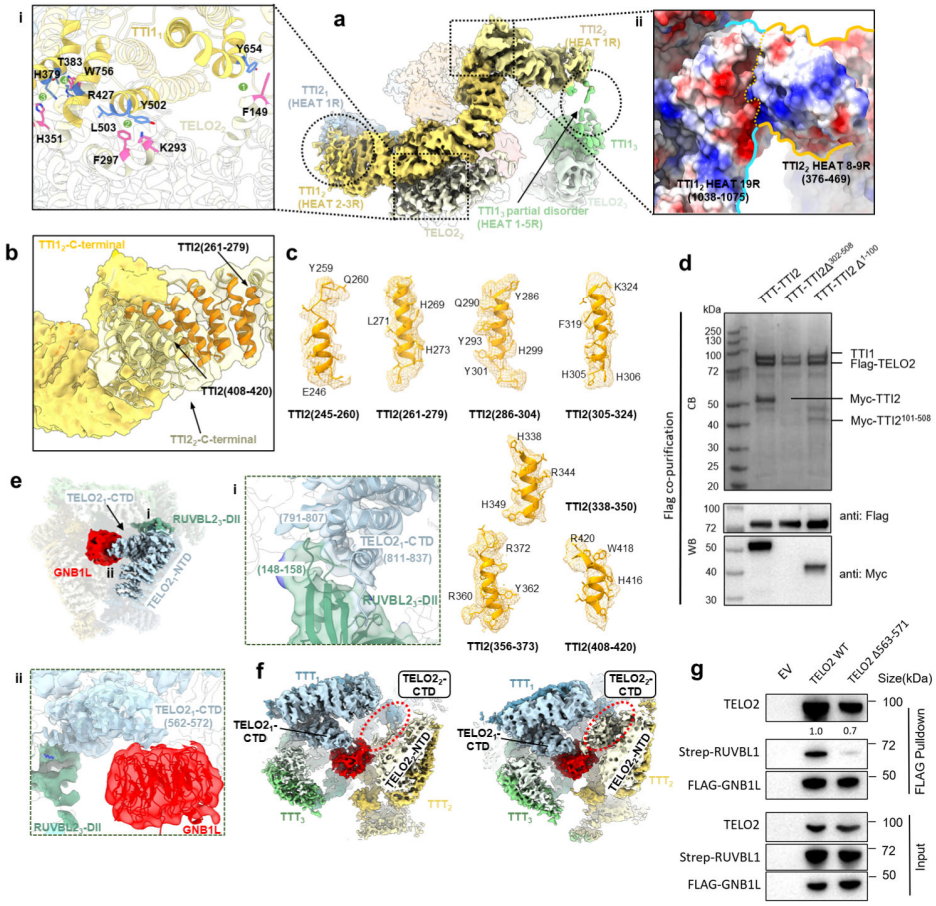

Figure 4 | Intra- and inter-TTT interface. a, Cryo-EM density map of copy-2 TTT and its interfaces with copy-1 TTI2 and copy-3 TTI1. Dashed circles mark two key contact sites involving different TTT copies, highlighting the interface between $TTI1_2$ (HEAT 2-3R) and $TTI2_1$ (HEAT 1R), and the interface between $TTI2_2$ (HEAT 1R) and the partially disordered $TTI1_3$ (HEAT 1-5R). Boxed regions correspond to insets i and ii: i, close-up view of key side-chain contacts at the TTI1-TELO2 interface, highlighting residues H351, H379, T383, W756, R427, L503, F297, K293, Y602 and Y654; ii, interaction between the C terminus of $TTI2_2$ (residues 376-469) and C terminus of $TTI1_2$ (residues 1038-1075), with the surface electrostatic potential illustrating their strong charge complementarity. **b,** Close-up view of the interface between $TTI2_2$ (beige surface rendered at 70% transparency) and the C terminus of $TTI1_2$

(light yellow surface rendered at 30% transparency). Approximately 35% of the TTI2 subunit which are depicted as dark orange ribbons exhibits side-chain density of sufficient quality to unambiguously identify bulky residues. **c,** Side-chain fitting for the seven helices (residues 245-420 of TTI2) highlighted in orange in panel b. Cryo-EM densities and the corresponding atomic models are shown, with bulky residues (for example, Leu, His, Phe, Arg, Tyr and Trp) explicitly labeled. The clear visualization of side-chain densities enables de novo model building of TTI2. **d,** Co-purification of wild-type TTI2 and its N-terminal (Δ1-100) and C-terminal (Δ302-508) truncation mutants with TELO2 and TTI1. FLAG-tagged TELO2 and untagged TTI1 were co-expressed with Myc-tagged TTI2 (wild-type or truncation mutants) in *Sf9* cells, and FLAG-purified fractions were analyzed by Coomassie blue staining and western blotting. **e,** Multivalent interactions mediated by the TELO2 C-terminal domain (CTD). Left: cryo-EM density map showing $TELO2_1$-CTD engaging TTI1, GNB1L, and the DII domain of $RUVBL2_3$. (i) Close-up of the $TELO2_1$-CTD-$RUVBL2_3$-DII interface; $TELO2_1$-CTD segments (791-807 and 811-837) directly interact with $RUVBL2_3$-DII (148-158). (ii) Close-up showing another $TELO2_1$-CTD core region (562-572) directly contacts GNB1L (red). **f,** Comparison of $TELO2_2$ CTD densities between two distinct conformational states, revealing its pronounced structural heterogeneity within the TTT_2 subcomplex. **g,** FLAG-GNB1L, Strep-RUVBL1/2, and untagged TTT (wild-type or Δ563–571 TELO2) were co-expressed in Sf9 insect cells and subjected to anti-FLAG pull-down. Eluates were analyzed by Western blotting. EV, empty vector control. FLAG-GNB1L served as the bait loading control. Relative band intensities were quantified by densitometry and normalized to the TELO2 WT condition (set to 1.0). Blots shown are representative of three independent biological replicates (n=3).

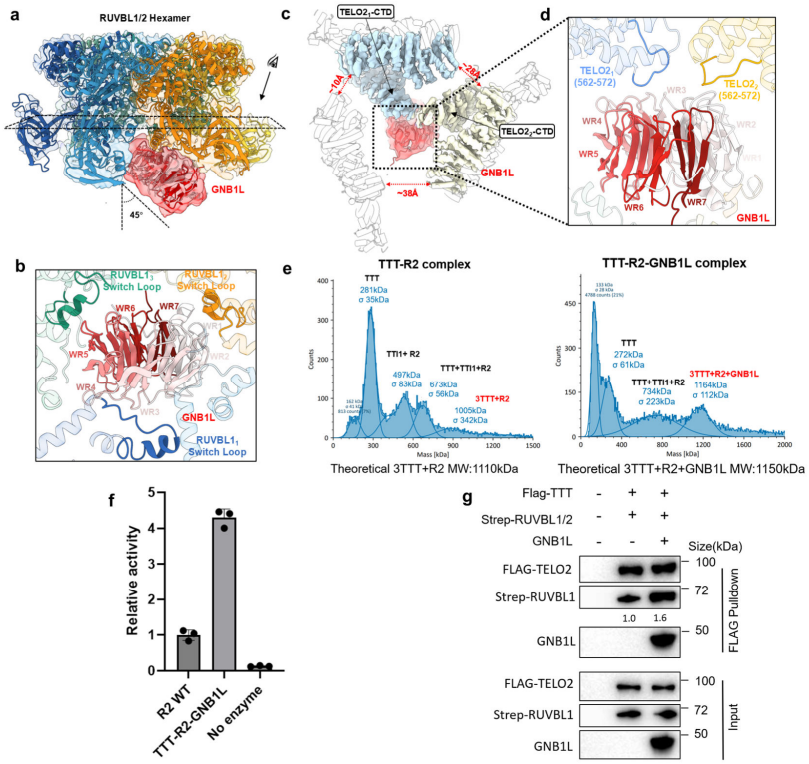

Fig.5| Structural and functional role of GNB1L in TTT-RUVBL1/2-GNB1L complex. a, Side view of the RUVBL1/2 heterohexamer bound to GNB1L. The atomic model is fitted into an 80% transparent cryo-EM density map, with the tilt angle of GNB1L indicated. The dashed line marks the cross-sectional plane corresponding to the view in b. **b,** Interface between the WD40 repeat domain of GNB1L and the Switch Loops of three RUVBL1 subunits, viewed along the cross-section indicated in a. **c,** Bottom view of the TTT-RUVBL1/2-GNB1L complex. Cryo-EM densities with colored surfaces highlighting the direct interface between two TELO2 subunits (copies 1 and 2) and GNB1L. The remaining components are displayed as a transparent model. Red arrows indicate the variation in distances among the three TELO2 subunits. **d,** Close-up view of the interface between the two TELO2 subunits and GNB1L. **e,** Single-molecule mass photometry analysis of TTT-RUVBL1/2(R2) incubation mixtures with or without GNB1L. Mass photometry histograms of the TTT-R2 and TTT-R2-GNB1L complexes (50 nM). Peaks are annotated with

composition, molecular mass, and associated error; the theoretical molecular mass of the intact complex is indicated for reference. **f,** In vitro ATPase activity of isolated RUVBL1/2 (R2 WT) and the co-purified TTT–R2–GNB1L complex. Reactions were performed with constant R2 concentrations, and a no-enzyme control was included as background. Relative activities were normalized to R2 WT (set to 1.0). Data are shown as means with individual data points from three technical replicates; error bars represent s.d. **g,** FLAG-tagged TELO2, TTI1, and TTI2 (TTT) were co-expressed with Strep-tagged RUVBL1/2 in Sf9 insect cells with or without untagged GNB1L. Cell lysates were subjected to anti-FLAG pull-down, and the eluates were analyzed by Western blotting. FLAG-TELO2 served as the bait loading control. Relative band intensities were quantified by densitometry and normalized to the TTT–R2 condition (set to 1.0). Blots shown are representative of three independent biological replicates (n=3).